Title: Grain-boundary-rich Pt nanoparticle assembly for catalytic hydrogen sensing at room temperature

Authors: Xin Geng,[1]† Shuwei Li,[2,3,4]† Jaeyoung Heo,[5]† Yi Peng,[1] Wenhui Hu,[6] Yanchao Liu,[7] Jier Huang,[6] Yang Ren,[8] Dongsheng Li,[5,]* Liang Zhang,[2,3,4,]* Long Luo[1,]*

Affiliations:

[1] Department of Chemistry, Wayne State University; Detroit, Michigan 48202, USA

[2] Center for Combustion Energy, Tsinghua University; Beijing,100084, China,

[3] School of Vehicle and Mobility, Tsinghua University; Beijing, 100084, China,

[4] State Key Laboratory of Automotive Safety and Energy; Beijing, 100084, China,

[5] Physical and Computational Sciences Directorate, Pacific Northwest National Laboratory; Richland, WA 99352, USA.

[6] Department of Chemistry, Marquette University; Milwaukee, Wisconsin 53201, United States

[7] Department of Industrial and Systems Engineering, Wayne State University; Detroit, Michigan 48202, USA

[8] Department of Physics, City University of Hong Kong; Hong Kong SAR, China

*Corresponding authors. Emails: dongsheng.li2@pnnl.gov; zhangbright@tsinghua.edu.cn; long.luo@wayne.edu

† These authors contributed equally to this work

Abstract: We report a facile method of synthesizing grain-boundary(GB)-rich platinum nanoparticle assembly. GBs are formed between platinum nanoparticles during their random collision and attachment in solution driven by water electrolysis. The GB-rich nanoparticle assembly exhibits ~400-fold higher catalytic hydrogen oxidation rate than platinum nanoparticles before assembly, enabling catalytic hydrogen sensing at room temperature without external heating. Our sensor also demonstrates fast response/recovery (~7 s at >1% H_2), nearly no signal variation during a 280-hour-long stability test, and high selectivity toward hydrogen over 36 interference gases. Furthermore, this sensor can be easily fabricated from commercial thermometers at a low cost (< $5 per unit). Theoretical calculation results reveal that the high performance of GB-rich platinum nanoparticle assembly arises from tensile strain at the GBs.

One-Sentence Summary: Connected particles are better than isolated particles.

Main Text: Hydrogen gas (H_2) sensors play a critical role in the hydrogen economy due to the safety concerns associated with the production, distribution, and utilization of flammable H_2. The United States Department of Energy (DOE) has set targets for H_2 sensors, in terms of concentration range (0.1–10%), operating temperature (−30 to 80 °C), response time (<1.0 s), gas environment (ambient air; 10–98% humidity), and lifetime (>10 years). (*1*) In addition to these metrics, H_2 sensors should be resistant to poisoning gases (e.g., hydrocarbons, CO, NO_2, H_2S, SO_x),(*2, 3*) inexpensive (< $40 per unit),(*4*) miniaturized, and power-efficient (< 1 W),(*5*) to ensure their effectiveness in various applications. There have been enormous efforts to develop high-performance and efficient H_2 sensors; however, it is incredibly challenging to meet all the target metrics. (*4-10*)

Typical commercially available H_2 sensors are of four types: electrochemical, catalytic, metal-oxide-semiconductor, and thermal conductivity, claiming over 90% of the H_2 sensor market. (*11, 12*) Among the four sensor types, catalytic sensors were found to be the most accurate and robust sensor type because they show little to no dependence of sensor output on the ambient parameters such as temperature, pressure, and humidity. (*11*) Catalytic sensors detect H_2 based on the exothermic oxidation reaction of H_2 with air on a catalyst surface (typically, Pt), which generates heat to change the electrical resistance of the catalyst for determining the H_2 concentration. However, due to the low activity of Pt catalysts in conventional catalytic H_2 sensors, a high operating temperature of ~500°C is often required (achieved by external heating), causing high power consumption (~0.5-3.0 W) and severe cross-sensitivity to other combustible gases, such as hydrocarbons, CO, etc. (*2, 11-13*) In addition, the performance of catalytic H_2 sensors is also affected following exposure to poisoning gases, such as H_2S and SO_2 (even at ppm level), which adsorb onto the Pt catalyst more strongly than H_2, thereby reducing the number of sites available to catalyze H_2 oxidation. (*13*) To overcome the limitations of catalytic H_2 sensors, prior efforts were focused on the miniaturization of the sensors, resulting in lower power consumption and faster response times. (*14-19*) However, the cross-sensitivity to combustible gases and susceptibility to catalyst poisoning is still not addressed.

Here, we report a grain-boundary(GB)-rich Pt nanoparticle (NP) assembly material that catalyzes H_2 oxidation in air at room temperature and exhibits low cross-sensitivity and negligible poisoning effect to common pollutant gases in the atmosphere (e.g., CO, NO_2, SO_2, H_2S, and NH_3) and various combustible organic gases and vapors (e.g., natural gas, alkanes, alkenes, alcohols, ketones, aldehydes, ethers, aromatic compounds, amine, and acetates). As illustrated in **Fig. 1A**, the GB-rich Pt NP assembly was synthesized by performing water electrolysis in an unbuffered, high-concentration (~1.7 μM) colloidal Pt NP solution. The local high pH of ~14 at the cathode assists the removal of citrate capping agents from the Pt NP surface (**fig. S1**). Gas bubbles generated during water electrolysis promote the random collisions of the destabilized Pt NPs after ligand removal, driving individual NPs to assemble into NP clusters, chains, networks, and eventually a macroscopic (sub-centimeter-sized) solid (**Fig. 1B-C, fig. S2**). Scanning transmission electron microscopic (STEM) images of Pt NPs and Pt NP assembly show no significant crystallite size change after the water-electrolysis-driven NP assembly (Pt NPs: 3.6 ± 0.5 nm and Pt NP assembly: 3.8 ± 0.7 nm, **Fig. 1B-C**). High-resolution TEM (HRTEM) and STEM images revealed that individual Pt NP building blocks in the Pt NP assembly were primarily connected by GBs. The representative GBs identified in the Pt NP assembly are Σ3 (111) twin boundaries, where two NPs share the low-energy {111} planes (e.g., NP1 and NP2 in **Fig. 1D**). (*20, 21*) We also observed Σ11 (113) GBs (**fig. S3**) and highly-disordered GBs (e.g., the GBs between the {111} plane of NP4 and the {200} plane of NP5 in **Fig. 1D**). It is worth noting that an interface-free structure can also form when two NPs oriented attach along the {111} planes (e.g., NP3 and NP4 in **Fig. 1D**).

The robust and practical nature of this electrosynthetic method was demonstrated by the gram-scale preparation of Pt NP assembly (**fig. S4**).

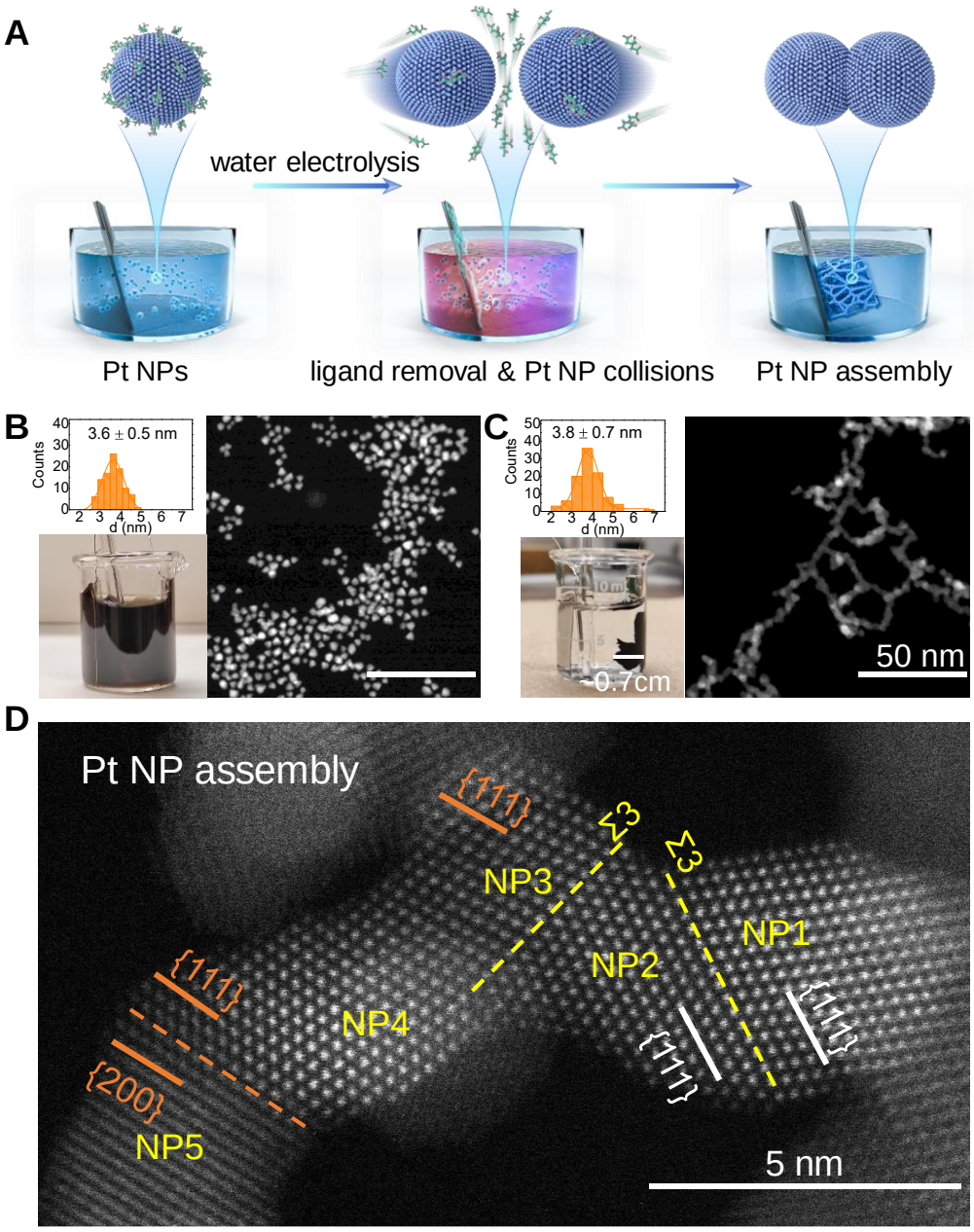

Fig. 1. Electrosynthesis of GB-rich Pt NP assembly from colloidal Pt NPs. (**A**) Schematic drawing of the NP assembly process driven by NP collisions under water electrolysis conditions that results in the formation of a macroscopic GB-rich Pt NP assembly. The local high pH near the cathode assists the citrate ligand removal from the Pt NP surface, and the electrogenerated gas bubbles promote the Pt NP collisions in solution. (**B** and **C**) Photographs, STEM images, and crystallite size distributions of (B) Pt NPs and (C) Pt NP assembly. (**D**) High-resolution STEM image of the GBs between the Pt NP building blocks in Pt NP assembly.

After synthesis, Pt NP assembly was subjected to critical point drying to prepare a dry powder (**fig. S5**). The electrochemically active surface area measured by hydrogen underpotential deposition of Pt NP assembly powder was 70 ± 1 cm^2/mg, ~80% lower than that of Pt NPs (340 ± 25 cm^2/mg, **fig. S6**), due to the loss of surface area when NPs are assembled. H_2 sensors were prepared by drop-casting a mixture of Pt NP assembly powder and ethanol onto a commercial thermocouple, followed by drying in air (**Fig. 2A**, insert). The sensor response is the temperature change (ΔT) of the catalyst-coated thermocouple upon exposure to H_2. We found that the Pt NP assembly was highly active for catalyzing H_2 oxidation in air. **Fig. 2A** shows that the sensor temperature rapidly increased from room temperature of ~22°C to ~360°C in ~10 s, after being exposed to a stream of 4% H_2 in air (*i.e.*, the lower explosive limit of H_2). Upon the removal of H_2, the sensor temperature quickly returned to room temperature within 10 s. ΔT decreases in response to stepwise decreasing H_2 concentrations (C_{H_2}) from 4% to 0.05%, yielding a linear relationship between ΔT and C_{H_2} at the logarithmic scale (**Fig. 2B**). In contrast, when the same loading (~1 mg) of Pt NPs was used to prepare a catalytic H_2 sensor, the sensor response is nearly negligible (< 1°C) even at C_{H_2} = 4% (**Fig. 2A**, insert, and **Fig. 2B**). The low catalytic activity of Pt NPs is not caused by their surface ligands blocking the active Pt sites. We ran control experiments using various Pt catalysts, including ligand-free Pt black with a surface area of 144 ± 5 cm^2/mg (**fig. S6**), Pt powder, Pt NPs after ligand removal, and Adams' catalyst (PtO_2) (**fig. S7**). None of them shows similar or even close catalytic activity to Pt NP assembly, suggesting the high catalytic activity of Pt NP assembly originates from its unique structure.

The response and recovery times of Pt NP assembly sensor, defined as the time to reach 90% of the total signal, were ~7 s at C_{H_2} > 1% and extended to ~1 min at 0.05% (**Fig. 2C**). Such negative dependence of sensor response and recovery times on C_{H_2} is common for H_2 sensors because low C_{H_2} is associated with a slow reaction rate between H_2 and the sensing material. (*4*, *5*, *7*) Even though the response time of Pt NP assembly sensor does not meet the DOE target of 1 s, it is still comparable to, or better than, the performance of existing catalytic H_2 sensors on the market (~10-30 s).(*22*, *23*) It is also important to point out that the Pt NP assembly sensor is capable of discriminating different H_2 concentrations in 1 s based on its transient temperature change (**fig. S8**). Due to the self-heating effect of Pt NP assembly during catalytic H_2 sensing, the sensor is operational over a wide ambient temperature range from −30°C to 80°C and a humidity range from 0 to 98% (**Fig. 2D-E, fig. S9**). In particular, when C_{H_2} > 2%, the sensor response, response and recovery times are not affected by the ambient temperature and humidity.

Most impressive is the low cross-sensitivity and anti-poisoning properties of Pt NP assembly. To evaluate these two metrics accurately, we adopted the interference/cross-sensitivity test protocol developed by the Safety Sensor Testing Laboratory at the DOE National Renewable Energy Laboratory with slight modifications (**fig. S10**).(*24*) **Fig. 2F** plots the percentage change of sensor temperature when exposed to 36 different interference gases, including CO, NO_2, SO_2, H_2S, NH_3, and various organic gas and vapors such as natural gas, hexane, benzene, formaldehyde, methanol, etc., in the absence and presence of 4% H_2 (see raw data in **fig. S10**). None of the interference gases has caused more than a 10% change in the sensor response, which is incredible because commercial catalytic H_2 sensors are known to suffer from severe cross-sensitivity to combustible gases and vapors (for example, the relative sensitivity for CH_4 and H_2 is about 1). (*23*) After being exposed to these interference gases, the sensor always returned to the initial state and produced the same response to H_2 as the calibrated value (**fig. S10**), indicating no irreversible

poisoning effect. Furthermore, the Pt NP assembly sensor exhibited high long-term stability. The sensor response remained constant during a 281-hour-long 288-test-cycles test (**Fig. 2G**, **fig. S11**). The relative standard deviation of sensor response was ~1% for $C_{H_2} \geq 1\%$. The variation in sensor response at a low C_{H_2} of 0.05% is possibly due to the slight room temperature fluctuation. Because the sensor readout is temperature, our H_2 sensors can be fabricated using any commercially available thermometers, including thermocouples, thermistors, and even liquid-in-glass laboratory thermometers (**fig. S12**), making the sensor inexpensive (as low as < $5 per unit) and easily miniaturized (size < 2 mm). Furthermore, we built a portable and wireless gas sensing system prototype that can be loaded onto a commercial drone and demonstrated its practicality for H_2 leak detection (**fig. S13**, **Movies S1, S2**).

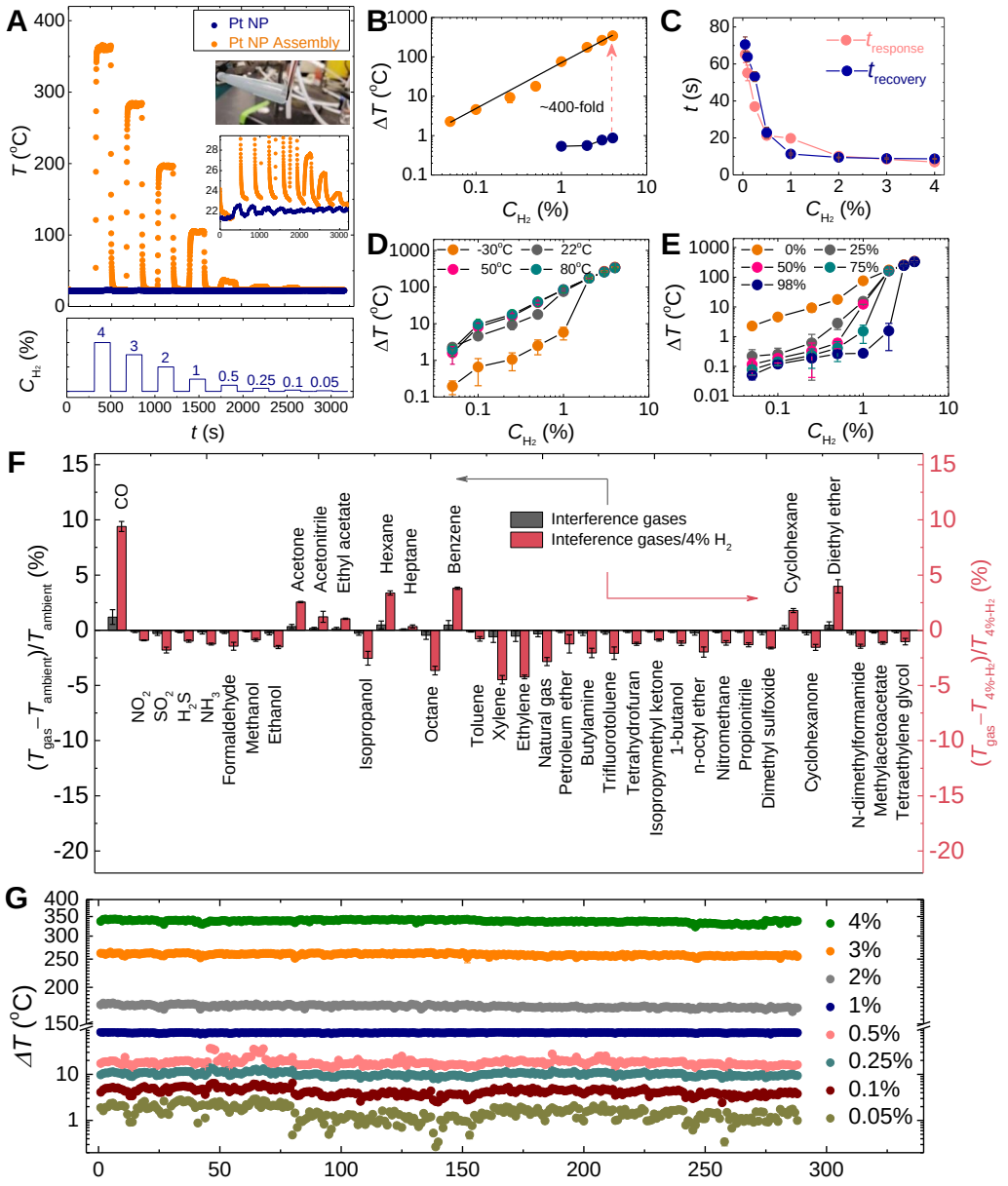

Fig. 2. Catalytic hydrogen sensing performance of Pt NP assembly at room temperature. (**A**) Temperature readout (*T*) of the catalytic hydrogen sensors built using Pt NPs (blue dots) and

Pt NP assembly (orange dots) in response to stepwise decreasing H_2 concentrations (C_{H_2}) from 4% to 0.05% in air at room temperature. The sensor temperature was recorded at 1 point per second. Inserts of (A) are photograph of a catalytic hydrogen sensor which is a J-type thermocouple coated with Pt NPs or Pt NP assembly, and an expanded view of the temperature response curves. (**B**) Sensor response ($\Delta T = T - T_{ambient}$, where $T_{ambient}$ is the ambient temperature) as a function of C_{H_2} for Pt NPs (blue dots) and Pt NP assembly (orange dots). (**C**) Response time ($t_{response}$) and recovery time ($t_{recovery}$) of the catalytic hydrogen sensor based on Pt NP assembly at various C_{H_2}. (**D** to **E**) Measured ΔT as a function of C_{H_2} when the Pt NP assembly-based sensor was operated at (D) an ambient temperature range from -30˚C to 80ºC and (E) a humidity range from 0% to 98%. (**F**) The percentage change of sensor response when exposed to 36 different interference gases (including CO, NO_2, SO_2, H_2S, NH_3, and various organic gases and vapors such as formaldehyde, methanol, etc.) in the absence and presence of 4% H_2 in air. The concentrations of the interference gases are 4%, except for NO_2 and SO_2 (4 ppm), ethylene (40 ppm), and H_2S (0.4 ppm). Error bars denote the standard deviations of at least three independent measurements. (**G**) Stability of the Pt NP assembly-based hydrogen sensor during a 280-hour-long 288-test-cycles test. In each cycle, C_{H_2} was decreased from 4% to 0.05% stepwise as in (A).

The high H_2 sensing performance of Pt NP assembly ultimately originates from its ability to efficiently catalyze H_2 oxidation even at room temperature. To understand how Pt NPs acquire such high activity after simple assembly, we compared the structures of Pt NPs and their assembly. X-ray absorption spectroscopy (XAS) results show different Debye-Waller factors (Pt NPs: 8.2 ±0.1 and Pt NP assembly:10±0.1, unit: 10^{-3} Å^2), suggesting that Pt NP assembly has higher local structural disorder than Pt NPs, but similar fitted Pt-Pt bond lengths (Pt NPs: 0.277 ± 0.002 nm; Pt NP assembly: 0.278 ± 0.002 nm) show no global lattice expansion or shrinkage (**fig. S14**). (*25*)

High-resolution x-ray diffraction (XRD) spectra of Pt NPs and Pt NP assembly in **Fig. 3A** present similar structural information as the XAS result. The XRD peaks of Pt NP assembly show broadening but no peak position change, relative to Pt NPs (**Fig. 3A-B**, **fig. S15**). Microstrain, crystallite size, and instrumental errors together determine XRD peak broadening but do not change the peak position. (*26-28*) The result in **Fig. 3A** suggests only increased microstrain is present in the Pt NP assembly, given the same instrumental errors and similar crystallite sizes of Pt NPs and Pt NP assembly (**Fig. 1B-C**). More interestingly, the XRD peak broadening for Pt NP assembly is anisotropic and asymmetric. Specifically, the peak broadening is more significant for the (111) peak (~17%) than others (e.g., 10% for (200) and 4% for (311) in **Fig. 3B**). The (111) XRD peak of Pt NP assembly was broadened by ~18% on the left side but ~10% on the right at half maximum. The anisotropy and asymmetry in peak broadening should be attributed to the dominance of Σ3 GBs that form along the {111}direction in Pt NP assembly and the tensile strain associated with these GBs.(*27*)

To further test this premise, we focused on the {111} planes and compared them with {200} planes using HRTEM (**Fig. 3C-D**). (*21*) We observed a lattice expansion of ~0.1 nm (i.e., tensile strain) in the Σ3 GB region of Pt NP assembly, shown by an offset between the TEM intensity profiles along the {111} planes of Pt NP and Pt NP assembly in **Fig. 3E**. In contrast, there was no apparent offset for their {200} profiles (**Fig. 3F**), possibly because {200} planes do not cross the GB. Based on TEM results, statistics of the *d*-spacing values for {111} and {200} planes also revealed that the *d*-spacing of Pt NP assembly exhibited a broader (~20%) distribution than Pt NPs, but their averaged spacings for {111} and {200} are almost the same: 0.226/0.225 nm and

0.195/0.196 nm, respectively (**Fig. 3G, fig. S16**), consistent with the observed XRD peak broadening for Pt NP assembly.

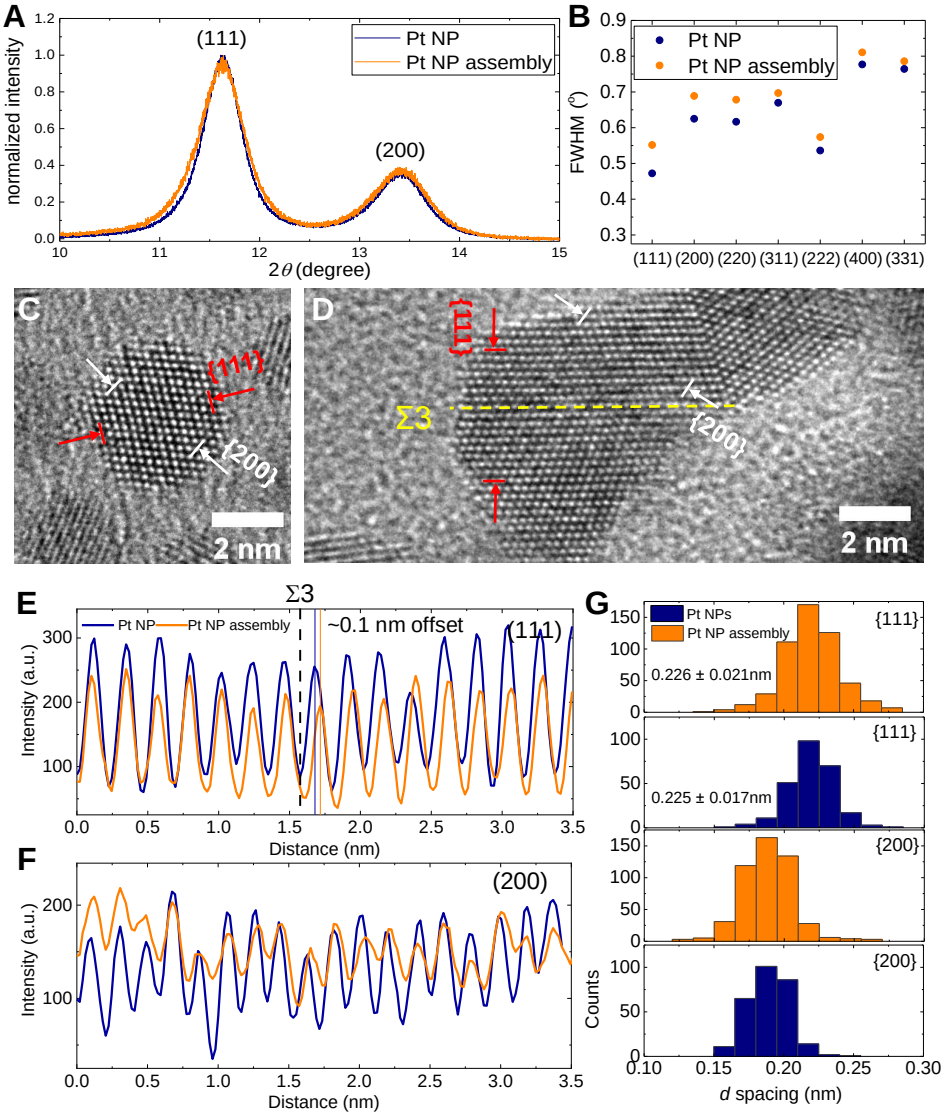

Fig. 3. Structural characterization of the GBs in Pt NP assembly. (**A**) High-resolution XRD spectra of Pt NPs and Pt NP assembly showing the (111) and (200) diffraction peaks. (**B**) Full width at half maximum (FWHM) of the XRD peaks for Pt NPs and Pt NP assembly. (**C-D**) HRTEM images of (A) Pt NP and (B) Pt NP assembly near a Σ3 GB. (**E-F**) The integrated pixel intensities of Pt NP and Pt NP assembly along (C) {111} and (D) {200} spacing directions. The peaks and valleys represent the atoms and gaps, respectively. The spacings of Pt {111} and Pt {200} planes were averaged over 3 atomic layers for high accuracy as labeled in (A) and (B). The lattice expansion at the Σ3 GB along the {111} direction leads to an offset between the intensity profiles of Pt NP and Pt NP assembly in (C). (**G**) Statistics of *d* spacings for the (111) and (200) facets, analyzed under the TEM pixel size of 0.0149 nm, shows Pt NP assembly has a similar mean value as Pt NP assembly but a broader distribution of *d* spacings than NPs (for (111), standard deviation: 0.021 vs 0.017 nm; for (200), standard deviation: 0.019 vs 0.015 nm).

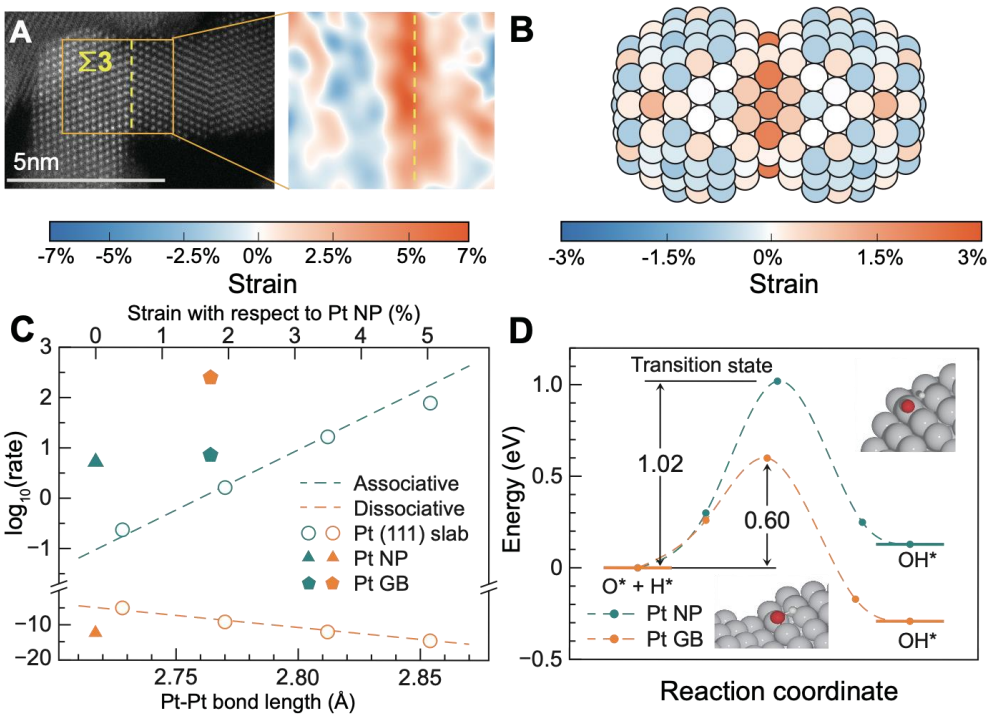

Fig. 4. Effect of GB on the catalytic hydrogen oxidation performance. (**A**) High-resolution STEM image of a Σ3 grain boundary between two Pt NPs in Pt NP assembly and its strain mapping near the grain boundary. (**B**) Calculated strain distribution in a Σ3 GB model (formed between two Pt_{201} NPs). The strain values are referenced to the isolated Pt_{201} NP (111) facet. (**C**) Calculated hydrogen oxidation rate on Pt (111) slabs with different Pt-Pt bond lengths (circles), isolated Pt_{201} NP (111) facet (triangles), and the Σ3 GB (pentagons). The associative and dissociative reaction pathways are marked green and orange, respectively. (**D**) Calculated minimum energy path of the rate-determining step in the dissociative pathway: O* + H* → OH*, on the Pt_{201} NP (111) facet and the Pt_{383} Σ3 GB. Insets show the corresponding transition states on NP and GB.

We further quantitatively analyzed the strain field near GBs in the Pt NP assembly from atomic-resolution STEM images using a geometric phase analysis algorithm.(*29*) **Fig. 4A** shows a tensile strain of up to 7% along the x-axis direction (i.e., the direction normal to {111} planes) is localized at a Σ3 (111) GB. Density functional theory (DFT) calculations performed on a Σ3 GB model formed between two Pt_{201} NPs confirmed the presence of tensile strain near the Σ3 GB (**Fig. 4B**, **fig. S17-18**). We further studied the two possible H_2 oxidation mechanisms over Pt (111) surface: associative and dissociative pathways (**fig. S19**).(*30*) DFT results in **Fig. 4C** and **fig. S19-20** show that the associative pathway dominates for Pt (111) slabs and Pt_{201} NP (111) facet, owing to its lower energy barrier at the rate-determining step (*i.e.*, OOH* formation, 0.38~0.42 eV, **Table S1**) than that of the dissociative pathway (O_2* dissociation: 0.54~0.72 eV or OH* formation: 0.75~1.02 eV, **Table S2**). Furthermore, we found a substantial enhancement of the associative H_2 oxidation rate due to the tensile strain on Pt (111) surfaces (green circles in **Fig. 4C**). Such enhancement was also observed for Pt GB with tensile strain relative to isolated Pt NP (green pentagon vs triangle in **Fig. 4C**). More excitingly, we discovered the GB also extensively reduced the activation barriers of O_2* dissociation to merely 0.008 eV (**Table S2**, **fig. S21**) and subsequent

hydrogenation of atomic O* to 0.60 eV (**Fig. 4D**), greatly accelerating H_2 oxidation through the dissociative pathway as well (orange pentagon, **Fig. 4C**).

This work demonstrates a facile and scalable approach for synthesizing a GB-rich Pt NP assembly and its practical use as an exceptionally high-performance catalytic hydrogen sensor that operates at room temperature. Furthermore, given the recently discovered high activities of GBs for other catalytic reactions such as CO_2 electroreduction and methane activation,(*31-33*) this synthetic approach will be powerful for studying the activity at GBs between NPs because the crystallite size of the NP precursors is largely retained in the NP-assembly, making the comparison between the activities with and without GBs straightforward.

References and Notes

1. U.S. Department of Energy, Energy Efficiency and Renewable Energy (EERE), Fuel Cell Technologies Office. *Multi-Year Research, Development, and Demonstration Plan, 2011–2020. Section 3.7 Hydrogen Safety, Codes and Standards (EERE, 2015).*
2. V. Palmisano *et al.*, Selectivity and resistance to poisons of commercial hydrogen sensors. *Int. J. Hydrogen Energy* **40**, 11740-11747 (2015).
3. V. Palmisano *et al.*, Evaluation of selectivity of commercial hydrogen sensors. *Int. J. Hydrogen Energy* **39**, 20491-20496 (2014).
4. W.-T. Koo *et al.*, Chemiresistive Hydrogen Sensors: Fundamentals, Recent Advances, and Challenges. *ACS Nano* **14**, 14284-14322 (2020).
5. I. Darmadi, F. A. A. Nugroho, C. Langhammer, High-Performance Nanostructured Palladium-Based Hydrogen Sensors—Current Limitations and Strategies for Their Mitigation. *ACS Sensors* **5**, 3306-3327 (2020).
6. T. Hübert, L. Boon-Brett, G. Black, U. Banach, Hydrogen sensors–a review. *Sens. Actuators B: Chem.* **157**, 329-352 (2011).
7. R. M. Penner, A Nose for Hydrogen Gas: Fast, Sensitive H2 Sensors Using Electrodeposited Nanomaterials. *Acc. Chem. Res.* **50**, 1902-1910 (2017).
8. F. A. A. Nugroho *et al.*, Metal–polymer hybrid nanomaterials for plasmonic ultrafast hydrogen detection. *Nat. Mater.* **18**, 489-495 (2019).
9. F. Favier, E. C. Walter, M. P. Zach, T. Benter, R. M. Penner, Hydrogen sensors and switches from electrodeposited palladium mesowire arrays. *Science* **293**, 2227-2231 (2001).
10. F. Yang, S.-C. Kung, M. Cheng, J. C. Hemminger, R. M. Penner, Smaller is faster and more sensitive: the effect of wire size on the detection of hydrogen by single palladium nanowires. *ACS Nano* **4**, 5233-5244 (2010).
11. L. Boon-Brett, J. Bousek, P. Moretto, Reliability of commercially available hydrogen sensors for detection of hydrogen at critical concentrations: Part II – selected sensor test results. *Int. J. Hydrogen Energy* **34**, 562-571 (2009).
12. L. Boon-Brett *et al.*, Identifying performance gaps in hydrogen safety sensor technology for automotive and stationary applications. *Int. J. Hydrogen Energy* **35**, 373-384 (2010).
13. T. Hübert, L. Boon-Brett, G. Black, U. Banach, Hydrogen sensors – A review. *Sens. Actuators B: Chem.* **157**, 329-352 (2011).
14. E.-B. Lee *et al.*, Micromachined catalytic combustible hydrogen gas sensor. *Sens. Actuators B: Chem.* **153**, 392-397 (2011).
15. A. Harley-Trochimczyk *et al.*, Platinum Nanoparticle Loading of Boron Nitride Aerogel and Its Use as a Novel Material for Low-Power Catalytic Gas Sensing. *Adv. Funct. Mater.* **26**, 433-439 (2016).

16. D. Del Orbe Henriquez *et al.*, Pt Nanostructures Fabricated by Local Hydrothermal Synthesis for Low-Power Catalytic-Combustion Hydrogen Sensors. *ACS Applied Nano Materials* **4**, 7-12 (2020).
17. X. Liu, H. Dong, S. Xia, Micromachined catalytic combustion type gas sensor for hydrogen detection. *Micro Nano Lett* **8**, 668-671 (2013).
18. R. E. Cavicchi *et al.*, Micro-differential scanning calorimeter for combustible gas sensing. *Sens. Actuators B: Chem.* **97**, 22-30 (2004).
19. A. Harley-Trochimczyk *et al.*, Catalytic hydrogen sensing using microheated platinum nanoparticle-loaded graphene aerogel. *Sens. Actuators B: Chem.* **206**, 399-406 (2015).
20. M. Song *et al.*, Oriented attachment induces fivefold twins by forming and decomposing high-energy grain boundaries. *Science* **367**, 40 (2020).
21. H. Grimmer, W. Bollmann, D. H. Warrington, Coincidence-site lattices and complete pattern-shift in cubic crystals. *Acta Crystallogr. A* **30**, 197-207 (1974).
22. M. Krawczyk, J. Namiesnik, Application of a catalytic combustion sensor (Pellistor) for the monitoring of the explosiveness of a hydrogen-air mixture in the upper explosive limit range. *J. Autom. Methods Manag. Chem.* **25**, 115-122 (2003).
23. RAE Systems, Inc., *RAE Systems Technical Note TN-114, Sensor Specifications and Cross-Sensitivities. Page 5-6.*
24. U.S. Department of Energy, National Renewable Energy Laboratory (NREL), Safety Sensor Testing Laboratory, *Standard Hydrogen Test Protocols, Pages 8-9, (2011).*
25. F. D. Vila, J. J. Rehr, H. H. Rossner, H. J. Krappe, Theoretical x-ray absorption Debye-Waller factors. *Phys. Rev. B* **76**, 014301 (2007).
26. R. Chattot *et al.*, Surface distortion as a unifying concept and descriptor in oxygen reduction reaction electrocatalysis. *Nat. Mater.* **17**, 827-833 (2018).
27. T. Ungár, Microstructural parameters from X-ray diffraction peak broadening. *Scr. Mater.* **51**, 777-781 (2004).
28. K. Venkateswarlu, A. Chandra Bose, N. Rameshbabu, X-ray peak broadening studies of nanocrystalline hydroxyapatite by Williamson–Hall analysis. *Phys. B: Condens. Matter* **405**, 4256-4261 (2010).
29. M. J. Hÿtch, E. Snoeck, R. Kilaas, Quantitative measurement of displacement and strain fields from HREM micrographs. *Ultramicroscopy* **74**, 131-146 (1998).
30. L. Qi, J. Yu, J. Li, Coverage dependence and hydroperoxyl-mediated pathway of catalytic water formation on Pt (111) surface. *J. Chem. Phys.* **125**, 054701 (2006).
31. W. Huang *et al.*, Steam-created grain boundaries for methane C–H activation in palladium catalysts. *Science* **373**, 1518-1523 (2021).
32. R. G. Mariano, K. McKelvey, H. S. White, M. W. Kanan, Selective increase in CO_2 electroreduction activity at grain-boundary surface terminations. *Science* **358**, 1187-1192 (2017).
33. C. W. Li, J. Ciston, M. W. Kanan, Electroreduction of carbon monoxide to liquid fuel on oxide-derived nanocrystalline copper. *Nature* **508**, 504-507 (2014).

Acknowledgments

Funding: This research was supported mainly by the U.S. Department of Energy (DOE), Office of Science, Office of Basic Energy Sciences, through Award # 78705. L.L., X. G., and Y. P. acknowledge support from National Science Foundation under award CHE-1943737. L.Z. and S.L. acknowledge support from the National Natural Science Foundation of China

(NSFC) under grant No. 22103047 and startup fund from Tsinghua University. W.H. and J.H. thank the support from National Science Foundation (DMR-1654140). This research used resources of the Advanced Photon Source; a DOE Office of Science User Facility operated for the DOE Office of Science by Argonne National Laboratory under Contract No. DE-AC02-06CH11357. The TEM work was supported by the DOE Office of Science, Office of Basic Energy Sciences, Early Career Research program under Award KC0203020:67037, and was conducted in the William R. Wiley Environmental Molecular Sciences Laboratory (EMSL), a national scientific user facility sponsored by the DOE Office of Biological and Environmental Research and located at Pacific Northwest National Laboratory (PNNL). PNNL is a multiprogram national laboratory operated for the DOE by Battelle under Contract No. DE-AC05-76RL01830.

Author contributions: X.G. and L.L. conceptualized the project. L.L., L.Z., and D.L. supervised the project. X.G. performed the majority of the experiments. S.L. conducted the theoretical simulation. J.H. and D.L. collected the HRTEM images and analyzed the GBs. X.G., Y.P., W.H., Y.L., J.H., and Y.R. contributed to the material characterization and analysis. L.L., X.G., L.Z., S.L., J.H., and D.L. collectively wrote the manuscript.

Competing interests: A U.S. provisional patent application (no. 63/278,451) based on the technology described in this work was filed on 11 Nov 2021 by L.L. and X.G. at Wayne State University. Authors declare that they have no competing interests.

Data and materials availability: All data are available in the main text or supplementary materials.

Supplementary Materials

Materials and Methods

Figs. S1 to S21

Tables S1 to S4

Movies S1 to S2

DFT-calculated optimal adsorption configurations and transition state geometries